MATERIALS SCIENCE

Springtail-inspired superomniphobic surface with extreme pressure resistance

Geun-Tae Yun[1]*, Woo-Bin Jung[1]*, Myung Seok Oh[2], Gyu Min Jang[3], Jieung Baek[2], Nam Il Kim[3], Sung Gap Im[2,4], Hee-Tae Jung[1,4†]

Both high static repellency and pressure resistance are critical to achieving a high-performance omniphobic surface. The cuticles of springtails have both of these features, which result from their hierarchical structure composed of primary doubly reentrant nanostructures on secondary microgrooves. Despite intensive efforts, none of the previous studies that were inspired by the springtail were able to simultaneously achieve both high static repellency and pressure resistance because of a general trade-off between these characteristics. We demonstrate for the first time a springtail-inspired superomniphobic surface displaying both features by fabricating a hierarchical system consisting of serif-T–shaped nanostructures on microscale wrinkles, overcoming previous limitations. Our biomimetic strategy yielded a surface showing high repellency to diverse liquids, from water to ethanol, with a contact angle above 150°. Simultaneously, the surface was able to endure extreme pressure resulting from the impacts of drops of water and of ethylene glycol with $We \gg 200$, and of ethanol with $We \sim 53$, which is the highest pressure resistance ever reported. Overall, the omniphobicity of our springtail-inspired fabricated system was found to be superior to that of the natural springtail cuticle itself.

INTRODUCTION

Springtails are small soil-dwelling arthropods that have remarkable cuticles with intrinsically omniphobic surfaces displaying both static repellency and pressure resistance to impacts of drops such as raindrops. The geometry of their cuticles has been evolutionarily adapted to avoid complete wetting by water and organic liquids, features critical for their survival because they respire through the skin. For springtails, static repellency induces self-cleaning, which maintains dry cuticles, while pressure resistance plays a significant role in providing resistance to dripping liquids. These unique characteristics result from the hierarchical structures of the cuticle, composed of mushroom-shaped nanostructures as primary granules and microscale grooves as secondary granules (Fig. 1A) (1–4). It has been recently reported that the nanoscale doubly reentrant primary granules play a critical role in omniphobicity because they can provide energetically stable pinning points with liquids having low surface tensions (1, 3). Although reentrant structures have been applied on the microscale to achieve static omniphobicity, a hierarchical omniphobic surface inspired by the springtail with both static repellency and high robustness to liquid pressure has yet to be realized. Previously reported omniphobic surfaces have not simultaneously achieved both features because of a general trade-off between these characteristics (5–8). Here, we took a significant step toward overcoming the limitations of previous biomimetic omniphobic surfaces.

RESULTS

Design of artificial springtail cuticle

To emulate the springtail cuticle, we designed an artificial springtail cuticle composed of "primary serif-T–shaped nanostructures on a secondary microscale wrinkled substrate." First, we fabricated serif-T–shaped nanostructures (see the dashed box of Fig. 1B), each composed of a "T"-shaped doubly reentrant head and pillar underneath, by combining nanoimprinting and secondary sputtering lithographic (SSL) techniques (Fig. 1B) (9, 10). We designed this structure to have the doubly reentrant feature of the primary granules of the springtail cuticle. A square packed nanopattern of ~400-nm-diameter gold dots separated from one another by ~400 nm was prepared on a polystyrene (PS) substrate by carrying out conventional nanoimprinting (fig. S1) (9, 11). Note that different types of metals or semiconductors instead of gold can be used for SSL, providing that the different metals can be deposited onto the substrate and are processable. After selectively etching the PS substrate vertically to a ~100-nm depth by carrying out anisotropic reactive ion etching (RIE) with oxygen (O_2) plasma, we deposited an additional 20-nm-thick gold layer on the entire substrate using e-beam sputtering. Then, a secondary sputtering technique was used to fabricate an ultrathin gold layer (~15 nm) onto the vertically etched sidewall of the PS substrate by carrying out Ar^+ ion bombardment (10). Finally, we produced PS pillars underneath the doubly reentrant head by O_2 RIE selective etching. The final serif-T–shaped structure, composed of a doubly reentrant head and PS pillar underneath, is depicted in the red-dashed box of Fig. 1B.

We emulated the microgrooves of the springtail cuticle, which serve as secondary granules, by generating microscale wrinkles with a specified wavelength and amplitude (Fig. 1C). The wrinkles were generated by reducing the areas of multiple layers having different Young's modulus values, with this reduction in area accomplished by heating the shrinkable PS substrate above its glass transition temperature (12–14). Note that the serif-T shape and dimensions of the nanostructures on the substrate were not changed during the wrinkling. To accomplish this maintenance, we embedded the serif-T arrays into

[1]National Laboratory for Organic Opto-Electronic Materials, Department of Chemical and Biomolecular Engineering (BK-21 Plus), Korea Advanced Institute of Science and Technology, Daejeon 305-701, South Korea. [2]Functional Thin Film Laboratory, Department of Chemical and Biomolecular Engineering, Korea Advanced Institute of Science and Technology, Daejeon 305-701, South Korea. [3]Combustion Laboratory, Department of Mechanical Engineering, Korea Advanced Institute of Science and Technology, Daejeon 305-701, South Korea. [4]KAIST Institute for NanoCentury, Daejeon, South Korea.
*These authors contributed equally to this work.
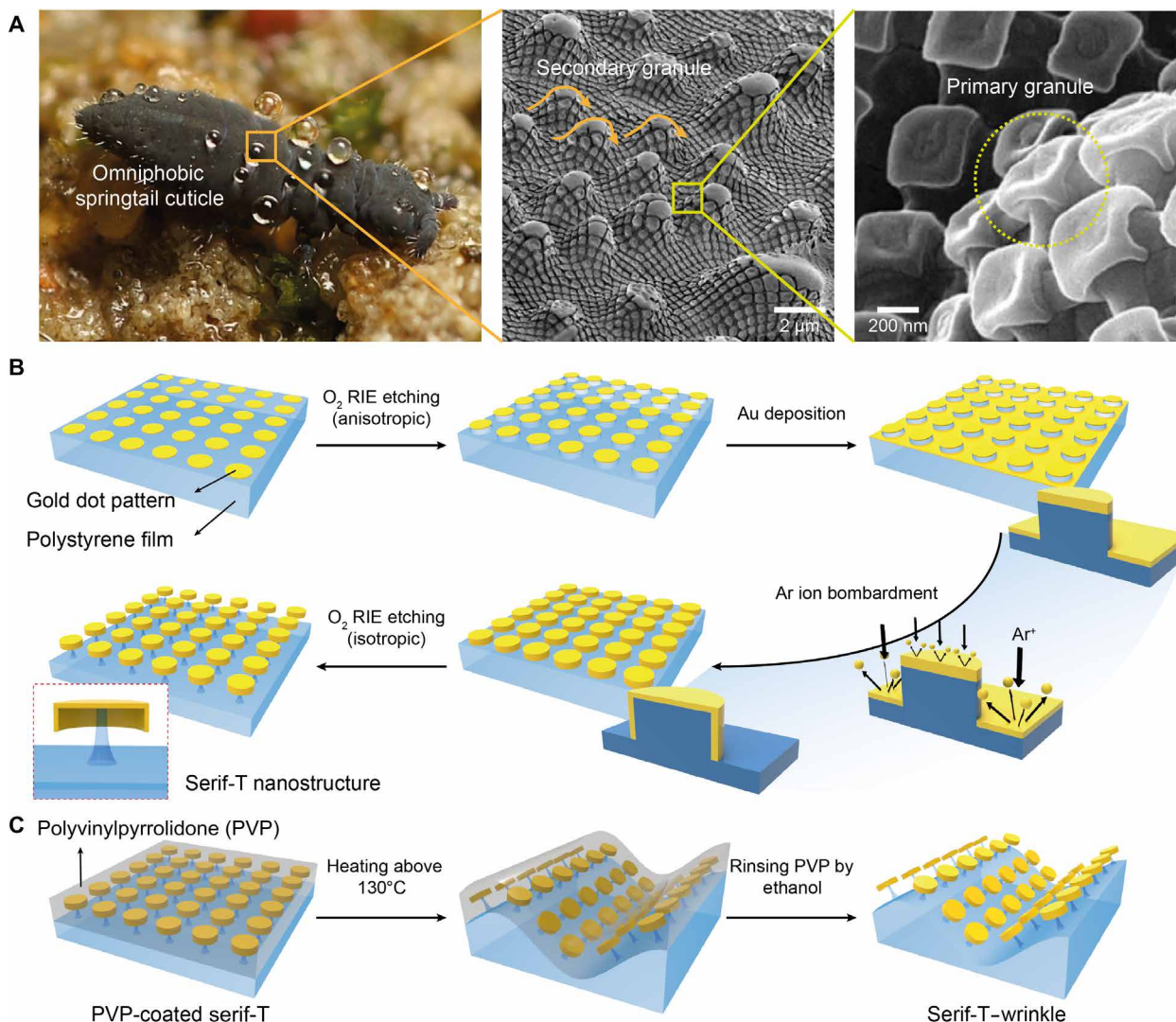†Corresponding author. Email: heetae@kaist.ac.kr

Fig. 1. Rational design of a hierarchical system inspired by the springtail cuticle. (**A**) Photograph (courtesy of B. Valentine) of a springtail displaying liquid repellency and resistance to high-pressure raindrops in a flooded habitat (left). SEM images showing the hierarchical system in a springtail cuticle composed of primary and secondary granules (middle and right panels). (**B**) Schematic of the steps used to fabricate serif-T–shaped nanostructures. Nanoimprinting and the SSL method were used here. The serif-T–shaped nanostructures were made with ~400-nm-diameter dots and ~ 400-nm spacing between the dots, both dimensions similar to those for the primary granules of springtail cuticles. (**C**) Scheme to fabricate microscale wrinkles via heat-induced shrinkage after nanostructure fabrication.

polyvinylpyrrolidone (PVP), which served both as a sacrificial skin layer and a protecting layer (*15*, *16*). Then, we heated the PVP-embedded serif-T–shaped nanostructures on the PS substrates at above 135°C to generate the microscale wrinkles. We modulated the wrinkle wavelength by simply controlling the concentration of the PVP solution and the magnitude of the applied areal strain. After using ethanol to rinse off the PVP, the hierarchical system with serif-T–shaped structures on a wrinkled substrate was fabricated over a large area. Last, to mimic the low surface energy, high uniformity, and continuity of the lipid-rich envelope on the outermost surface of the springtail cuticle, all of which contribute to the nonwetting nature (*17*), we coated a ~40-nm-thick layer of the fluorinated polymer, poly-(3,3,4,4,5,5,6,6,7,7,8,8,9,9,10,10,10-heptadecafluorodecyl methacrylate) (PHFDMA), onto the artificial springtail surface using the initiated chemical vapor deposition (iCVD) method (fig. S2) (*17*–*19*).

System realization with one-to-one correspondence design

Inspection of top and cross-sectional scanning electron microscopy (SEM) images of the hierarchical system (Fig. 2) showed it to be well fabricated and to mimic the biological structure. A magnified SEM image (inset of Fig. 2A) displays details of the serif-T–shaped nanostructures, each consisting of a doubly reentrant head and pillar underneath. We designed the average diameter (d ~ 365 nm) and sidewall length (~100 nm) of the head of the serif-T–shaped structure in our artificial springtail to match well the dimensions of the primary granules on springtails. However, we designed the average height of the pillars to be ~600 nm, greater than that (~300 nm) of the springtail itself. Our experimental results and previous reports indicated higher pillars to be better suited for pinning liquids between adjacent nanostructures (*6*, *8*). The value of ~600 nm was the maximum pillar height in our design that simultaneously provided a mechanical stability during the
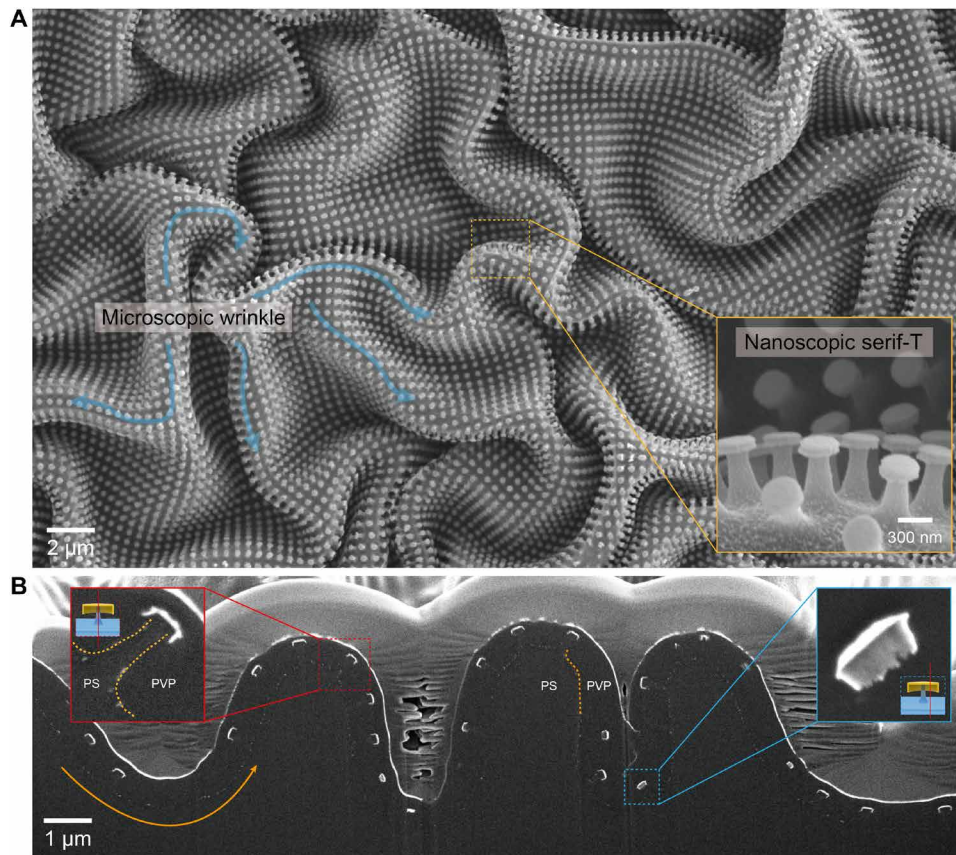
Fig. 2. Morphologies of serif-T–shaped nanostructures on a microscale-wrinkled substrate. (**A**) SEM image of a fabricated hierarchical system with serif-T–shaped nanostructures on a microscale-wrinkled substrate. Inset SEM image shows details of a few serif-T–shaped nanostructures. (**B**) Cross-sectional view of the hierarchical serif-T system imaged by using a FIB-SEM. The inset in the red box shows a magnified view of a serif-T–shaped structure with a well-made pillar. The inset in the blue box shows only the head of this structure, with the head made hollow to provide a doubly reentrant shape.

wrinkling process and high static repellency (fig. S3). We designed our wrinkles to have an average wavelength (distance between valleys) of ~4.2 µm, which matched the period of secondary granules for the springtail (3 to 5 µm) (*1*, *2*). Overall, our artificial design (Fig. 2A) closely emulated the shapes and dimensions of the primary and secondary granules in the springtail.

A cross-sectional view of our fabricated product, acquired using a focused ion beam scanning electron microscope (FIB-SEM), confirmed that the heads of the serif-T–shaped structures remained intact despite the structures being attached to a microscale-wrinkled substrate (Fig. 2B). To produce the specific specimens analyzed using the FIB-SEM, we cut PVP-embedded samples by an ion beam after deposition of gold (~50 nm) and platinum (~1 µm) layers that were used to enhance image contrast. Inspection of the magnified FIB-SEM image (inset of Fig. 2B, red box) clearly showed that each of the serif-T–shaped nanostructures consisted of a PS pillar (dark gray) and gold head (white) with distinct doubly reentrant features. The PS pillar was discriminated by the contrast difference between PVP (black) and PS (dark gray), arising from the different electron densities of the two polymers (*20*). Inspection of the cross-sectional view of the head (inset SEM image of Fig. 2B, blue box) verified the presence of empty space between the sidewall and pillar, which is critical geometry to maintain stable composite interface between liquid and vapor by providing pinning points (*4*, *5*, *8*). These observations in-

dicated our fabrication approach to be an effective biomimetic strategy for capturing the evolutionarily adapted design of the springtail cuticle into an engineered system.

Relations between static repellency and structural features

Our artificial springtail surface showed outstanding static omniphobicity. We compared three different nanostructures (disk-, overhang-, and serif-T–shaped) on microscale wrinkles with various morphologies (Fig. 3) to find the combination that yielded the greatest static repellency in our design. We fabricated disk-shaped nanostructures by embossing a polymer dot pattern on a gold-deposited PS substrate and etching the exposed gold (fig. S1). We obtained reentrant overhang nanostructures by carrying out isotropic RIE etching of some of the disk-shaped nanostructures (fig. S4). Magnified SEM images clearly showed successful fabrications of hierarchical systems with disk-, overhang-, and serif-T–shaped structures on wrinkled substrates (inset images of Fig. 3A). We controlled the wrinkle wavelength by selecting the appropriate PVP concentration and magnitude of applied areal strain during shrinkage. The applied strain was determined by measuring the biaxial degree of shrinkage [ε; $\varepsilon = (A_0 - A_f)/A_0$, where A_0 and A_f represent projected areas before and after strain relief, respectively], which was controlled by changing the duration of heating for shrinkage. As the strain was increased, the wrinkle wavelength decreased and its amplitude increased (fig. S5).
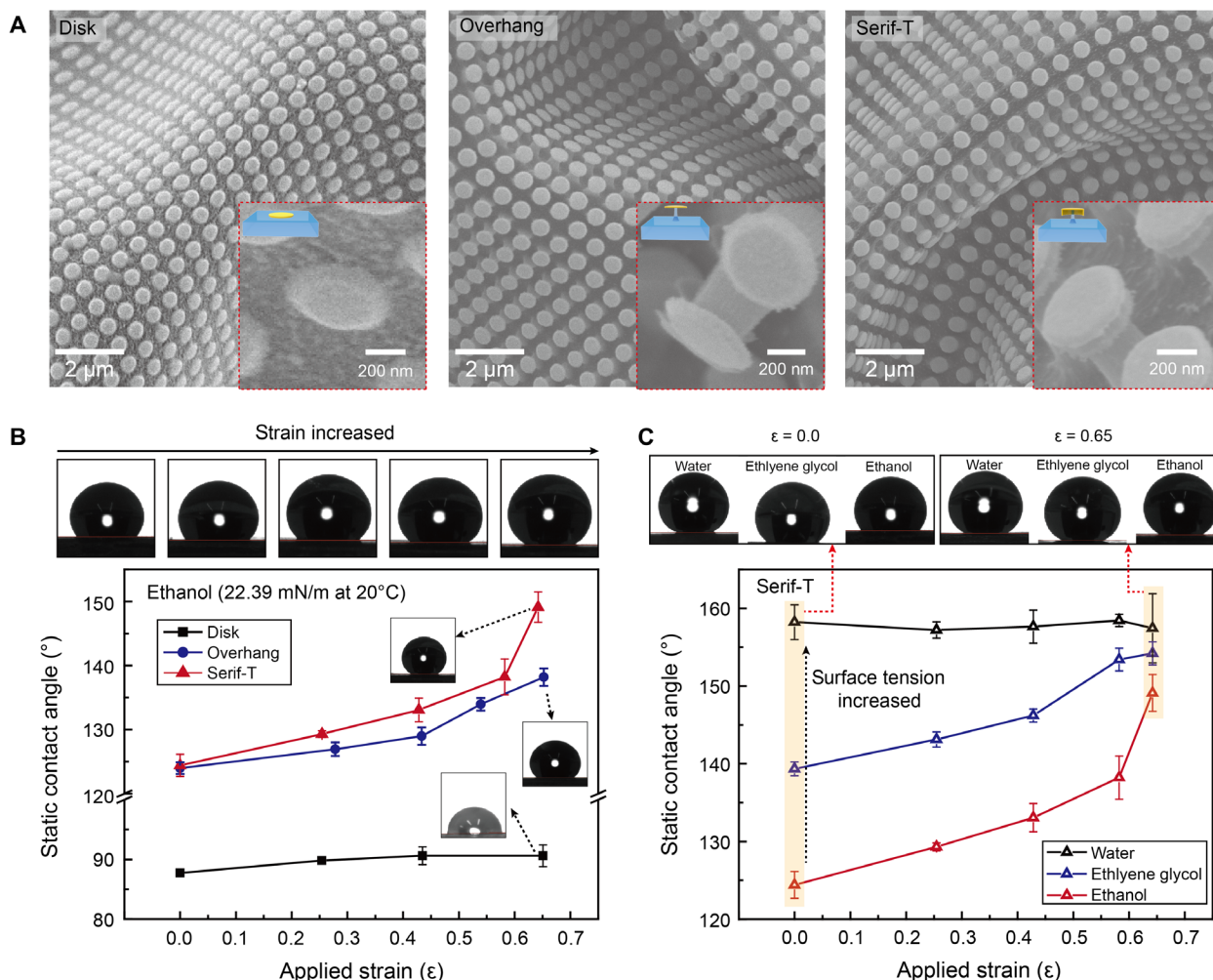
Fig. 3. Morphological control of nano- and microstructures and corresponding static repellency. (**A**) Hierarchical systems with different kinds of nanostructures. (**B**) Static contact angles of ethanol on hierarchical systems with control nanostructures. (**C**) Static contact angles of test liquids (water, ethylene glycol, and ethanol) on the hierarchical serif-T–shaped nanostructures system.

The product containing the serif-T–shaped nanostructures showed better static omniphobicity than did the product containing the disk-shaped structures and that containing the overhang-shaped structures. The serif-T–shaped nanostructures yielded better performances for three different tested liquids, specifically water (σ = 71.99 mN/m), ethylene glycol (σ = 47.3 mN/m), and ethanol (σ = 22.39 mN/m). The superiority of the serif-T–shaped nanostructure was observed for the measurement of ethanol contact angles. Figure 3B and fig. S6 show contact angles of ethanol for the three different nanostructures and various applied strains (and hence various wrinkle wavelengths). As expected, the disk-shaped nanostructures yielded relatively poor static repellency (CA ~ 90°) at all strains because of the absence of reentrant structures (fig. S7) (5–8). While the static contact angles of the overhang- and serif-T–shaped systems were similar (~124°) for the flat surface (ε = 0), for the wrinkled (ε = 0.65) surface the serif-T–shaped nanostructures showed a contact angle of 150°, whereas the overhang-shaped nanostructures showed a contact angle of only 138°. This enhanced repellency of the serif-T–shaped system was attributed to the doubly reentrant geometry

with stable air pockets between adjacent nanostructures (4, 5). Thus, compared to the other tested shapes, the serif-T was a more suitable and effective geometry for nanostructures on a wrinkled surface to repel low-surface-tension liquids such as ethanol.

In addition to the effect of the nanostructures, the dimensions of the microstructure were also found to influence static repellency. We measured the static contact angles of water, ethylene glycol, and ethanol on the product containing the serif-T–shaped nanostructures as a function of areal strain (Fig. 3C). The static repellency of the low-surface-tension liquids ethylene glycol and ethanol was significantly increased as the areal strain on the substrate was increased. Comparisons of snapshots showing the contact angles resulting from the serif-T–shaped nanostructures on flat (ε = 0.0) and highly wrinkled (ε = 0.65) substrates supported the results obtained by direct observation of the contact angles (Fig. 3C). Because of the different surface tensions of ethylene glycol and ethanol, different contact angles on the flat surface were obtained (ε = 0.0): 138° for ethylene glycol and 124° for ethanol. However, as the strain was increased in each case to a wrinkled surface (ε = 0.65), the static repellency reached ~150° for both

liquids. In the case of water, the artificial hierarchical springtail with serif-T–shaped nanostructures was superhydrophobic (apparent contact angle ~160°) regardless of applied strain. On the basis of the above results, we concluded that a combination of serif-T–shaped nanostructures and highly wrinkled surface is the most beneficial for repelling low-surface-tension liquids.

Extreme pressure resistance of artificial springtail cuticle

The artificial springtail surface consisting of serif-T–shaped nanostructures on a wrinkled substrate showed extreme resistance to water, ethylene glycol, and ethanol at elevated hydrodynamic pressures. Both the serif-T–shaped nanostructures and wrinkled microstructures were confirmed to be crucial for the pressure resistance, although the presence of microwrinkles was found to be more important. Figure 4A shows the water spreading and bouncing-off behaviors as a function of Weber number (We) for disk-, overhang-, and serif-T–shaped nanostructures, each on a highly wrinkled surface ($\varepsilon = 0.7$). We is a dimensionless measure of pressure ($We = 2R_0\rho V_i^2/\sigma$, where V_i is the impact velocity, ρ is the density, and σ is the surface tension). Thus, high pressure resulting from the impact of a droplet would show a high value of We ([21]–[23]). In a water dropping test, a complete rebound (CR) of the water droplet was obtained for each of the disk, overhang, and serif-T systems in all tested We ranges from ~22 to ~220, indicating their high resistance to pressure by water droplet impact. Droplets were observed to fragment for high values of We (hollow symbols in the plots of Fig. 4A), consistent with previous reports indicating fragmentation resulting from unstable interfaces between liquid and air at high We impact ([24], [25]). On the other hand, the maximum spreading factor ($D_{max}^* = R_{max}/R_0$, where R_{max} is the maximum diameter of the spread drop and R_0 is the initial diameter of the drop) for the serif-T system was greater than those for the disk and overhang systems, indicating more effective drag reduction and lower contact angle hysteresis for the serif-T system ([26]–[28]). We further verified a high pressure resistance of the serif-T system by measuring the height to which a water drop jumped back up after impacting the surface of the system at a fixed We ~110 (Fig. 4B), with this height being an indicator of the energy remaining after spreading and retraction ([29]). This height was measured to be greater from the serif-T system than from the disk system, which implied less energy loss during spreading and retraction of a water droplet on the surface of the serif-T system. Thus, we found the serif-T–shaped nanostructures to exhibit greater pressure resistance and static repellency than the nanostructures with other shapes.

In addition, we found the pressure resistance of the artificial springtail surface to be strongly affected by the dimensions of the microwrinkles. Figure 4C shows the maximum spreading factor (D_{max}^*) as a function of We for various values of the strain ($\varepsilon = 0$, $\varepsilon = 0.4$, and $\varepsilon = 0.7$) applied to the serif-T system. D_{max}^* at We ~ 220 increased from 3.12 to 3.88 as the strain was increased from $\varepsilon = 0$ to $\varepsilon = 0.7$. While water droplets impacting highly wrinkled surfaces with three different nanostructures in Fig. 4A started to fragment from the same We ~ 120, serif-T–shaped nanostructures on surfaces subjected to various microstructures showed different fragmentation starting points (empty symbols in the plots of Fig. 4C). The highly wrinkled surface ($\varepsilon = 0.7$) showed fragmentation of water droplets at a smaller We ~ 132 than did the moderately wrinkled (We ~ 154) and flat (We ~ 198) surfaces, indicating that the highly wrinkled surface provided more air pockets than did the others (fig. S8). This observation supports the advantages of the highly wrinkled surface that can provide more air pockets, thus resulting in an earlier fragmentation starting

point and reduced contact fraction and friction on the surface. We also confirmed these results by comparing the heights to which drops with a We ~ 110 bounced after impacting the highly wrinkled surface (Fig. 4D).

We found wrinkles to be particularly important for system robustness to pressure. To compare the importance of the nanostructures to that of microscale wrinkles, we measured the value of contact time (time between initial impact and bouncing off) of water on three different sets of surfaces: (i) disk- and serif-T–shaped nanostructures each on flat surfaces, (ii) disk-shaped nanostructures on a flat surface and a highly wrinkled surface, and (iii) disk- and serif-T–shaped nanostructures on flat and highly wrinkled surfaces (Fig. 4E). Contact time indicates the overall affinity between the liquid and the surface, and thus, surfaces displaying short contact times have great advantages for surface robustness ([30]). Measurements of spreading factor ($D^* = R_t/R_0$, where R_t and R_0 are the spreading diameter at time t and at the initial state) of water (We ~ 220) as a function of time showed a 4.6-ms shorter contact time of a water droplet with the serif-T–shaped nanostructures on a flat surface than with the disk-shaped structures on a flat surface (Fig. 4E, left). We attributed this result to the presence of fine nanoscale air pockets formed around the serif-T–shaped nanostructures, resulting in a lower solid-liquid fraction and hence a lower contact angle hysteresis and friction. Disk-shaped nanostructures on a highly wrinkled surface ($\varepsilon = 0.7$) showed a 9.8-ms shorter contact time than did disk-shaped nanostructures on a flat surface (Fig. 4E, middle), indicating that the presence of microscale wrinkles is more important than the nanostructure for reducing the fraction of the surface contacting the liquid. Yet, the combination of serif-T–shaped nanostructures and highly wrinkled surface showed a contact time of ~10.2 ms, which was shorter than those of any of the other systems we tested (Fig. 4E, right). Notably, the shape of the plot of the spreading factor versus time for this combination was nearly symmetric and parabolic, that is, the water drop was in contact with this surface during spreading for about the same amount of time as during retraction, which was attributed to its extremely low friction and low contact angle hysteresis. Consequently, we found the system consisting of serif-T–shaped nanostructures on a highly wrinkled surface to show remarkable performance features, particularly low loss of energy and low contact time for an impacting water droplet on the surface.

The artificial springtail surface also showed outstanding levels of pressure resistance, even for ethylene glycol and ethanol. In previous studies, pressure resistance with regard to ethylene glycol and ethanol with high We has proven extremely difficult to achieve because of their low surface tension ([31]). In particular, achieving a robust omniphobic surface with respect to impacts from drops of these liquids with elevated hydrodynamic pressure is difficult and challenging ([32]).

Figure 5A shows outstanding bouncing of ethylene glycol drops off our artificial springtail surface consisting of serif-T–shaped nanostructures on microscale wrinkles. While the overhang-shaped nanostructures did yield a loss of resistance, which implies partial rebound (PR) and deposition (DEP) behaviors, as We was increased, the serif-T system yielded a high pressure resistance (that is, CR), even up to We ~ 287 (fig. S9). In particular, the influence of microscale wrinkles on pressure resistance was indicated by the different bouncing behaviors of ethylene glycol drops off on the flat ($\varepsilon = 0$) and highly wrinkled ($\varepsilon = 0.7$) surfaces each studded with the serif-T–shaped nanostructures. Although ethylene glycol drops collapsed on the flat surface studded with the serif-T nanostructures as the applied We was increased to greater than ~150 (Fig. 5A), these drops showed CR up to
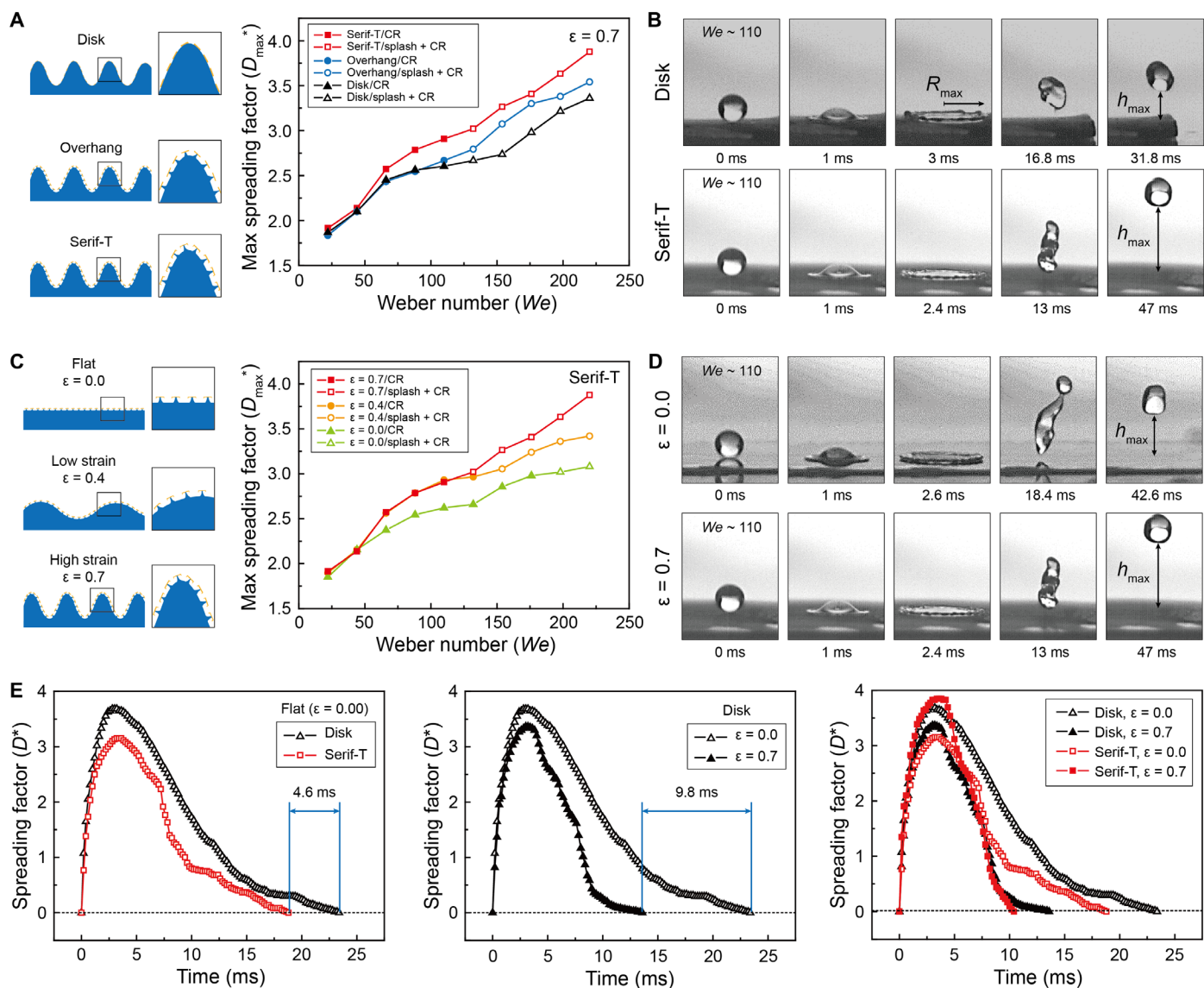
Fig. 4. Wetting resistance levels of the hierarchical systems to water drop impact. (A) Schematic figures of the hierarchical systems with different nanostructures, and plots of maximum spreading as a function of *We* for each of these systems. **(B)** Snapshots of water droplets interacting with two of the systems in (A) using *We* ~ 110. **(C)** Schematics of the serif-T system with different microstructure morphologies and plots of maximum spreading as a function of *We* for each of these systems. **(D)** Snapshots of water droplets interacting with two of the systems in (C) using *We* ~ 110. **(E)** Contact time analysis for various systems (*We* ~ 220).

We ~ 287 from the highly wrinkled surface studded with same nanostructures (Fig. 5B). Such CR implied that the highly wrinkled surface studded with the serif-T–shaped nanostructures did not experience the soaking at elevated pressure that the system containing these nanostructures on the flat surface did. We attributed this remarkable improvement to pressure loading dispersion into both the nanoscale and microscale air pockets, a smaller solid-liquid contact fraction, and wetting reversibility due to the presence of additional air pockets in the hierarchical system (*33*). By comparing contact times of ethylene glycol droplets on the highly wrinkled surface studded with the serif-T–shaped nanostructures for various values of *We*, we were able to show that ethylene glycol penetrated into the microgrooves as *We* was increased, which implied that the microscale air pockets were present

and work as a buffer layer for pressure dispersion under a load. Penetration of ethylene glycol into the microgrooves of wrinkles at high *We* likely caused the extended contact time, stickiness during retraction, and poor rebound of the liquid. In contrast, for water, contact time decreased as *We* was increased (fig. S10), attributed to an expected inability of water to penetrate into the microgrooves.

Extreme pressure resistance (*We* ~ 53) on the artificial springtail surface with ethanol, an extremely low surface tension liquid, was achieved (Fig. 5C). We finely controlled the applied *We* from ~13 to ~65 on serif-T systems subjected to three different levels of strain (ε = 0.0, 0.4, and 0.7) and, hence, displaying different degrees of wrinkling (zero, moderate, and high levels of wrinkling, respectively). While it is impossible for such a single-scale system of nanostructures
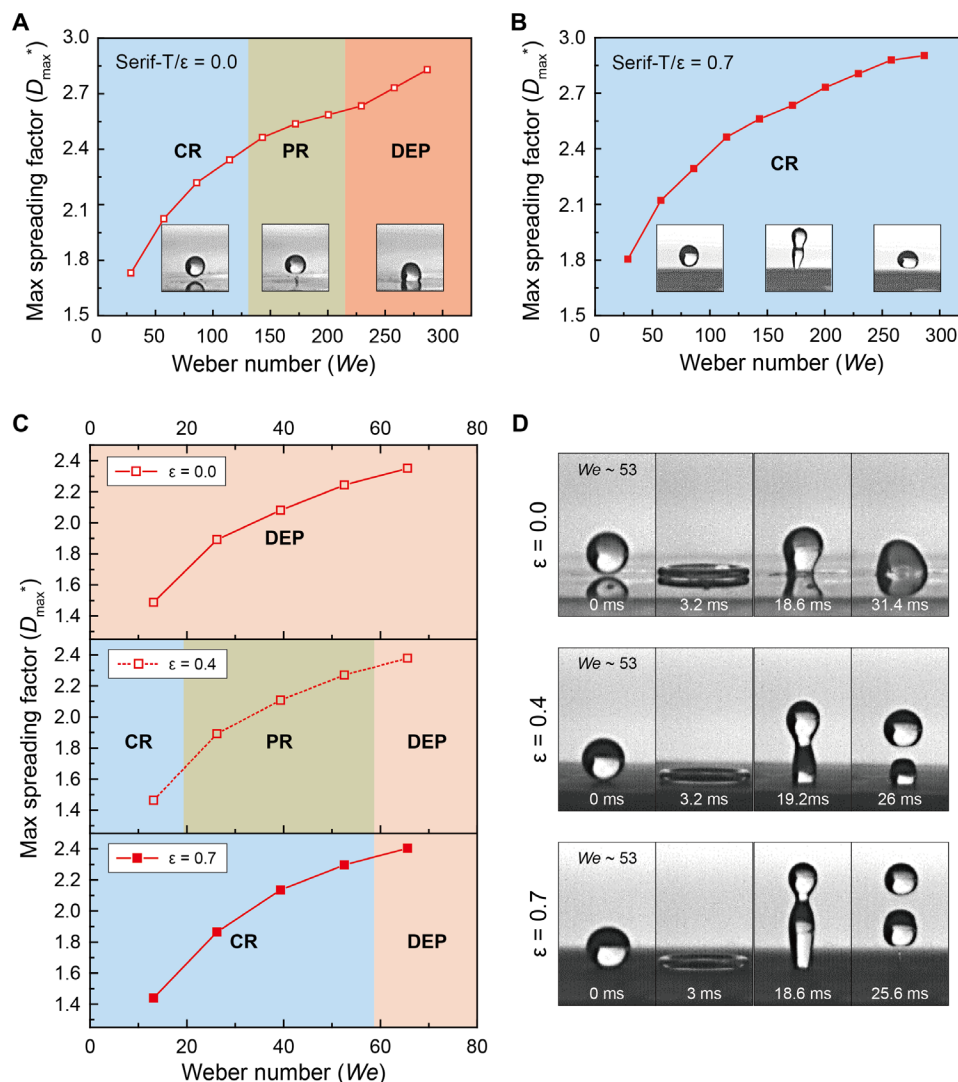
Fig. 5. Wetting resistance of hierarchical system to impacts by low-surface-tension liquids. Comparison of bouncing-off behaviors of ethylene glycol for serif-T nanostructure system on (**A**) flat and (**B**) highly wrinkled surfaces. Images of the interactions of ethylene glycol drops with these surfaces are shown. (**C**) Bouncing behaviors on the serif-T hierarchical system on different levels of microstructures subjected to various applied strains with ethanol impact (*We* from ~13 to 65). (**D**) Images of ethanol drops interacting with serif-T hierarchical systems with different microscale morphologies at *We* ~ 53.

to display extreme pressure resistance, in our hierarchical system, the serif-T–shaped nanostructures on microscale wrinkles resulting from ε = 0.4 and ε = 0.7 showed a remarkable enhancement in this resistance. By applying a moderate level of strain (ε = 0.4), ethanol droplets completely bounced off the resulting surface at *We* ~ 13 and showed PR and DEP over *We* ~ 25. The most impressive result was the CR of the ethanol drops up to *We* ~ 53 off the serif-T–shaped nanostructures on the highly wrinkled surface. It is worth emphasizing the advantage of using a hierarchical system rather than a microstructure-based single-scale system to achieve extremely high resistance even with the impact of liquids displaying very low surface tension. We attributed this significant enhancement for the hierarchical system to a distinct reduction of the solid-liquid contact fraction due to the presence of additional air pockets from valley-like microstructures and wetting reversibility. Ethanol drops were observed in snapshots to bounce to a greater extent off serif-T systems subjected to greater

applied strain (Fig. 5D). Our results, in particular those shown in Figs. 4 and 5, revealed our artificial springtail surface composed specifically of serif-T–shaped nanostructures on highly wrinkled surface to display not only high static omniphobicity (CA ~ 150°) but also extreme pressure resistance (*We* ~ 53) with low-surface-tension liquids.

DISCUSSION
The hierarchical system we designed showed outstanding performance in terms of both static omniphobicity and pressure resistance even with low-surface-tension liquids. These results were attributed to the presence of sufficient air pockets both between the serif-T–shaped nanostructures and in the microscale grooves that together can provide a highly stable Cassie-Baxter regime. In addition, the serif-T geometry with doubly reentrant features was highly effective at providing

a robust Cassie-Baxter regime, much more so than the other geometries despite their having the same air pocket dimensions. The microstructures resulting from the wrinkles effectively reduced the solid-liquid contact fraction of the entire surface, which was also highly important for achieving robustness. In addition, because the fragmentation of the liquids presumably originated from air layers at the solid-liquid interface, we concluded that the valley-like microstructures contained additional air pockets based on our observation of earlier commencement of fragmentation for the highly wrinkled surface as *We* increased (Fig. 4, A and C) (*24, 25*). Finally, the presence of additional air pockets in the grooves of the highly wrinkled surfaces helped to reduce energy loss during spreading and retraction on the surface after droplet impact, leading to the drops bouncing off the surface to a greater a height than from a flat surface. As a result, the artificial springtail surface, specifically the highly wrinkled surface studded with serif-T–shaped nanostructures, provided extreme pressure resistance with the liquids we tested.

In conclusion, we were inspired by the structures and properties of the cuticles of springtails to design and fabricate an artificial hierarchical system and verified its outstanding omniphobic characteristics. We fabricated this system by using a combination of lithographic tools and a wrinkling method. This fabrication for the most part yielded both the nanoscale and microscale features and the dimensions of these features as found in the springtail cuticle. In most existing omniphobic surfaces showing only features on the microscale, there has been an inevitable trade-off between static repellency and wetting resistance to pressure, with few investigations showing a stable Cassie-Baxter regime to both static repellency (apparent contact angle, low contact angle hysteresis) and pressure resistance (robustness upon being impacted with droplets at high velocity) (*32*). Our novel design showed high omniphobicity resulting from the doubly reentrant features of serif-T–shaped nanostructures and the hierarchical system. Although the role of the primary nanostructures of the springtail cuticle in omniphobicity is clear, the influence of microgrooves has yet to be properly elucidated. Hence, the inclusion of these microstructures in our hierarchical system may help to shed light on their role in the springtail system. Among the hierarchical systems we fabricated with different nanostructures, including disk-, overhang-, and serif-T–shaped structures, we demonstrated the serif-T–shaped nanostructure and a highly wrinkled surface to be the most advantageous. We attributed these results to these geometries being most effective at reducing the fraction of the surface in contact with the liquid and providing for a sufficient amount of air pockets. We believe this fabricated system to be one of the most optimally designed springtail-inspired systems for creating a superomniphobic surface with extreme pressure resistance.

MATERIALS AND METHODS

Surface structuring
See section S1 for the processes to fabricate the hierarchical omniphobic surfaces. The processes included nanoscale dot pattern formation, lithographic steps to tune the types of nanostructures, wrinkling, low surface energy polymer coating, and characterization, as described below in detail.

Nanodot pattern formation
A gold layer (40 nm) was deposited on a PS substrate by e-beam sputtering. To fabricate gold dot patterns over the area, polyvinylpyro-lidone prepatterns with 400-nm diameter were produced as the etching mask. Following etching of the gold layer, which was not covered by mask, and rinsing off the polymer, a metal pattern array with 400-nm diameter features 400 nm apart from each other was fabricated over the PS substrate. Schematic illustrations are depicted in fig. S1.

Types of nanostructure control
After nanoscale dot pattern formation on the PS substrate, the types of nanostructures can be tuned with different further lithographic processes including RIE, argon ion bombardment, and SSL. The types of nanostructures were designed as disk-, overhang-, and serif-T–shaped. For disk-shaped nanostructures, the nanoscale dot arrays were used as they were. In the case of the overhang-shaped nanostructures, the pillars underneath the gold dot patterns were made by O_2 RIE under low vacuum conditions ($\sim 10^{-2}$ torr) with O_2 [30 standard cubic centimeter per minute (sccm)] for 5 min and high vacuum conditions ($\sim 10^{-6}$ torr) with O_2 (30 sccm) for 3 min. The overall processes for disk- and overhang-shaped systems are described in fig. S4. In addition, extra SSL processes were added for serif-T–shaped nanostructures. To fabricate the sidewall of the doubly reentrant feature, the dot pattern array–formed PS substrate was etched vertically (anisotropic) by RIE under high vacuum ($\sim 10^{-6}$ torr) with O_2 (100 sccm) for 90 s. Then, an additional gold layer of 20-nm thickness was deposited by e-beam sputtering and argon bombardment under low energy (500 eV). In the SSL processes, the thin gold layer (~ 15 nm) of the sidewall was fabricated on vertically pre-etched PS. Details are described in section S1.

Wrinkling process
Heat-induced surface shrinkage was used for fabricating wrinkled surfaces over a large area. A PVP with ethanol solution was used for the upper layer and protecting layer for nanostructures at the same time. A 5 weight % PVP solution was coated over a structured surface by a spin coater. Afterward, heating in an oven at 135°C induced shrinkage of the PS substrate. By controlling the heating time, the applied areal strain ε ($\varepsilon = (A_0 - A_f)/A_0$, where A_0 and A_f represent projected areas before and after strain relief, respectively, was controlled.

Surface coating by iCVD
Low surface energy PHFDMA was deposited on the structured surface by an iCVD machine (Daeki Hi-Tech Co. Ltd). Both the monomer, 3,3,4,4,5,5,6,6,7,7,8,8,9,9,10,10,10-heptadecafluorodecyl methacrylate (HFDMA) (97%), and the initiator, tert-butyl peroxide (TBPO) (98%), were purchased from Sigma-Aldrich and used without any further purification. Both HFDMA and TBPO were loaded into separate source cylinders and introduced to the iCVD reactor at a flow rate of 1 sccm each. To obtain the target flow rate, TBPO was kept at room temperature while HFDMA was heated to 75°C before being introduced into the iCVD reactor. The pressure of the chamber was set to 80 mtorr. The temperature of the filament was set to 180°C, and the substrate temperature was 40°C. Contact with the heated filament activated the initiator molecules, creating radicals and inducing a chain reaction. The radical polymerization on the substrate surface continued until the filament was turned off and the flow of the monomer and initiator was stopped. The thickness of the polymer layer was monitored in situ by an He-Ne laser (JDS Uniphase). The thickness of the polymer layer was ~40 nm. A schematic illustration of the procedure is presented in fig. S2.

Morphology characterization

The morphologies of the system were observed by field emission SEM (SU-5000, Hitachi). In addition, for cross-sectional observation, FIB-SEM (Helios Nanolab 450 F1, Nanolab Technologies) was used.

Repellency tests

The repellency of the surfaces was tested with a selection of test liquids such as water, ethylene glycol, and ethanol. Apparent contact angles were measured at room temperature (20°C) for static repellency, and bouncing-off behaviors after droplet impact on the surface were observed by a high-speed camera to estimate the resistance to hydrodynamic pressure of droplets, as described below in detail.

Contact angle measurement

The apparent contact angle was measured by a contact angle system (Attention, KSV instruments). Test liquids were water, ethylene glycol, and ethanol. Droplets were deposited on a fabricated surface by a micropipette. The volume of droplets was 6 μl for all cases. Samples were hierarchical systems with disk-, overhang-, and serif-T–shaped nanostructures. The apparent contact angle was automatically decided by a computer program (OneAttention).

Droplet impact test

Bouncing-off behaviors after drop impact on fabricated surfaces were captured by a high-speed camera (Photron Mini UX50). Test liquids were water, ethylene glycol, and ethanol, the same as for apparent contact angle measurements. The syringe pump (Chemyx Fusion 100) released same volume of liquids to drop on the surface with constant speed. The height of the drop was controlled from 3 to 30 cm in the case of water and ethylene glycol (We from ~22 to ~220 for water and from ~29 to ~287 for ethylene glycol) to get different hydrodynamic pressures (We). On the other hand, ethanol was controlled finely from 1 to 5 cm (We from ~13 to ~65).

SUPPLEMENTARY MATERIALS

Supplementary material for this article is available at http://advances.sciencemag.org/cgi/content/full/4/8/eaat4978/DC1

Supplementary Text

Fig. S1. Schematic illustration of gold dot nanopattern fabrication on PS substrate by using conventional nanoimprinting.

Fig. S2. Schematic illustration of polymer with low surface energy (PHFDMA) coating on structured surface by iCVD.

Fig. S3. SEM images of nanostructures with different pillar etching condition.

Fig. S4. Schematic illustration of fabrication for hierarchical system with overhang (reentrant)– and disk-shaped nanostructures.

Fig. S5. Different morphologies of wrinkled surface with applied areal strain during wrinkling.

Fig. S6. Advancing and receding contact angles of ethanol on the three different nanostructures.

Fig. S7. Contact regimes of ethanol droplet on surface with disk-shaped nanostructures and contact angles of various liquids.

Fig. S8. Fragmentation observation of water droplet with different Weber number (We) on hierarchical system with serif-T–shaped nanostructures.

Fig. S9. Bouncing-off behaviors after ethylene glycol droplet impacts on highly wrinkled surface with overhang- and serif-T–shaped nanostructures.

Fig. S10. Contact time analysis of ethylene glycol and water on hierarchical serif-T–shaped nanostructures surface with various We.

Movie S1. Bouncing behavior of water on the different nanostructures.

Movie S2. Contact time comparison of water.

Movie S3. Bouncing test of ethylene glycol on the overhang and the serif-T wrinkles.

Movie S4. Bouncing test of ethanol on serif-T samples.

REFERENCES AND NOTES

1. R. Hensel, R. Helbig, S. Aland, A. Voigt, C. Neinhuis, C. Werner, Tunable nano-replication to explore the omniphobic characteristics of springtail skin. *NPG Asia Mater.* **5**, e37 (2013).
2. R. Helbig, J. Nickerl, C. Neinhuis, C. Werner, Smart skin patterns protect springtails. *PLOS ONE* **6**, e25105 (2011).
3. R. Hensel, C. Neinhuis, C. Werner, The springtail cuticle as a blueprint for omniphobic surfaces. *Chem. Soc. Rev.* **45**, 323–341 (2016).
4. R. Hensel, R. Helbig, S. Aland, H.-G. Braun, A. Voigt, Christoph Neinhuis, C. Werner, Wetting resistance at its topographical limit: The benefit of mushroom and serif T structures. *Langmuir* **29**, 1100–1112 (2013).
5. T. Liu, C.-J. Kim, Turning a surface superrepellent even to completely wetting liquids. *Science* **346**, 1096–1100 (2014).
6. A. Tuteja, W. Choi, M. Ma, J. M. Mabry, S. A. Mazzella, G. C. Rutledge, G. H. McKinley, R. E. Cohen, Designing superoleophobic surfaces. *Science* **318**, 1618–1622 (2007).
7. J. H. Kim, T. S. Shim, S.-H. Kim, Lithographic design of overhanging microdisk arrays toward omniphobic surfaces. *Adv. Mater.* **28**, 291–298 (2016).
8. A. Tuteja, W. Choi, J. M. Mabry, G. H. Mckinley, R. E. Cohen, Robust omniphobic surfaces. *Proc. Natl. Acad. Sci. U.S.A.* **105**, 18200–18205 (2008).
9. M. Li, J. Wang, L. Zhuang, S. Y. Chou, Fabrication of circular optical structures with a 20 nm minimum feature size using nanoimprint lithography. *Appl. Phys. Lett.* **76**, 673–675 (2000).
10. H.-J. Jeon, K. H. Kim, Y.-K. Baek, D. W. Kim, H.-T. Jung, New top-down approach for fabricating high-aspect-ratio complex nanostructures with 10 nm scale features. *Nano Lett.* **10**, 3604–3610 (2010).
11. B. Radha, S. H. Lim, M. S. M. Saifullah, G. U. Kulkarni, Metal hierarchical patterning by direct nanoimprint lithography. *Sci. Rep.* **3**, 1078 (2013).
12. J. A. Rogers, T. Someya, Y. Huang, Materials and mechanics for stretchable electronics. *Science* **327**, 1603–1607 (2010).
13. D.-Y. Khang, H. Jiang, Y. Huang, J. A. Rogers, A stretchable form of single-crystal silicon for high-performance electronics on rubber substrates. *Science* **311**, 208–212 (2006).
14. M. D. Huntington, C. J. Engel, A. J. Hryn, T. W. Odom, Polymer nanowrinkles with continuously tunable wavelengths. *ACS Appl. Mater. Interfaces* **5**, 6438–6442 (2013).
15. W.-K. Lee, J. Kang, K.-S. Chen, C. J. Engel, W.-B. Jung, D. Rhee, M. C. Hersam, T. W. Odom, Multiscale, hierarchical patterning of graphene by conformal wrinkling. *Nano Lett.* **16**, 7121–7127 (2016).
16. M. D. Huntington, C. J. Engel, T. W. Odom, Controlling the orientation of nanowrinkles and nanofolds by patterning strain in a thin skin layer on a polymer substrate. *Angew. Chem. Int. Ed. Engl.* **53**, 8117–8121 (2014).
17. J. Nickerl, M. Tsurkan, R. Hensel, C. Neinhuis, C. Werner, The multi-layered protective cuticle of Collembola: A chemical analysis. *J. R. Soc. Interface* **11**, 20140619 (2014).
18. K. K. S. Lau, K. K. Gleason, Initiated chemical vapor deposition (iCVD) of poly(alkyl acrylates): A kinetic model. *Macromolecules* **39**, 3695–3703 (2006).
19. K. K. S. Lau, K. K. Gleason, Initiated chemical vapor deposition (iCVD) of Poly(alkyl acrylates): An experimental study. *Macromolecules* **39**, 3688–3694 (2006).
20. W. Brostow, B. P. Gorman, O. Olea-Mejia, Focused ion beam milling and scanning electron microscopy characterization of polymer+metal hybrids. *Mater. Lett.* **61**, 1333–1336 (2007).
21. C. Ukiwe, D. Y. Kwok, On the maximum spreading diameter of impacting droplets on well-prepared solid surfaces. *Langmuir* **21**, 666–673 (2005).
22. Y. C. Jung, B. Bhushan, Dynamic effects of bouncing water droplets on superhydrophobic surfaces. *Langmuir* **24**, 6262–6269 (2008).
23. J. B. Lee, S. H. Lee, Dynamic wetting and spreading characteristics of a liquid droplet impinging on hydrophobic textured surfaces. *Langmuir* **27**, 6565–6573 (2011).
24. P. Tsai, M. H. W. Hendrix, R. R. M. Dijkstra, L. Shui, D. Lohse, Microscopic structure influencing macroscopic splash at high Weber number. *Soft Matter* **7**, 11325–11333 (2011).
25. H. Kim, C. Lee, M. H. Kim, J. Kim, Drop impact characteristics and structure effects of hydrophobic surfaces with micro- and/or nanoscaled structures. *Langmuir* **28**, 11250–11257 (2012).
26. N. Laan, K. G. de Bruin, D. Bartolo, C. Josserand, D. Bonn, Maximum diameter of impacting liquid droplets. *Phys. Rev. Appl.* **2**, 044018 (2014).
27. R. S. Voronov, D. V. Papavassiliou, L. L. Lee, Slip length and contact angle over hydrophobic surfaces. *Chem. Phys. Lett.* **441**, 273–276 (2007).
28. J. P. Rothstein, Slip on superhydrophobic surfaces. *Annu. Rev. Fluid Mech.* **42**, 89–109 (2010).
29. Y. Nam, H. Kim, S. Shin, Energy and hydrodynamic analyses of coalescence-induced jumping droplets. *Appl. Phys. Lett.* **103**, 161601 (2013).
30. J. C. Bird, R. Dhiman, H. M. Kwon, K. K. Varanasi, Reducing the contact time of a bouncing drop. *Nature* **503**, 385–388 (2013).

31. J. B. Lee, D. Derome, A. Dolatabadi, J. Carmeliet, Energy budget of liquid drop impact at maximum spreading: Numerical simulations and experiments. *Langmuir* **32**, 1279–1288 (2016).

32. A. R. Bielinski, M. Boban, Y. He, E. Kazyak, D. H. Lee, C. Wang, A. Tuteja, N. P. Dasgupta, Rational design of hyperbranched nanowire systems for tunable superomniphobic surfaces enabled by atomic layer deposition. *ACS Nano* **11**, 478–489 (2017).

33. T. Verho, J. T. Korhonen, L. Sainiemi, V. Jokinen, C. Bower, K. Franze, S. Franssila, P. Andrew, O. Ikkala, R. H. Ras, Reversible switching between superhydrophobic states on a hierarchically structured surface. *Proc. Natl. Acad. Sci. U.S.A.* **109**, 10210–10213 (2012).

Citation: G.-T. Yun, W.-B. Jung, M. S. Oh, G. M. Jang, J. Baek, N. I. Kim, S. G. Im, H.-T. Jung, Springtail-inspired superomniphobic surface with extreme pressure resistance. *Sci. Adv.* **4**, eaat4978 (2018).